Oscillations and confluence in three-magnon scattering of ferromagnetic resonance

Tao Qu, Alex Hamill, R. H. Victora, and P. A. Crowell

Oscillations and confluence in three-magnon scattering of ferromagnetic resonance

Tao Qu,[1] Alex Hamill,[2, *] R. H. Victora,[1] and P. A. Crowell[2]

[1]*Department of Electrical and Computer Engineering,*
University of Minnesota, Minneapolis, MN, 55455, USA
[2]*School of Physics and Astronomy,*
University of Minnesota, Minneapolis, MN, 55455, USA

Abstract

We have performed a time-resolved and phase-sensitive investigation of three-magnon scattering of ferromagnetic resonance (FMR) over several orders of magnitude in excitation power. We observe a regime that hosts transient oscillations of the FMR magnon population, despite higher-order magnon interactions at large powers. Also at high powers, the scattering generates 180° phase shifts of the FMR magnons. These phase shifts correspond to reversals in the three-magnon scattering direction, between splitting and confluence. These scattering reversals are most directly observed after removing the microwave excitation, generating coherent oscillations of the FMR magnon population much larger than its steady-state value during the excitation. Our model is in strong agreement with these findings. These findings reveal the transient behavior of this three-magnon scattering process, and the nontrivial interplay between three-magnon scattering and the magnons' phases.

Magnons are the quanta of collective spin excitations. Their phase degree of freedom, highly nonlinear behavior [1–17], and long lifetimes make them an active subject in fundamental research [18–21] and research towards next-generation microwave and information technology [22–29]. A magnon mode's population (hereafter referred to as its amplitude) can be excited above a threshold value such that it becomes unstable, returning to the threshold value through three-magnon splitting [30]. This nonlinear process is referred to as the first-order Suhl instability.

The zero-wavevector magnon mode corresponds to ferromagnetic resonance (FMR) and has a dramatically low threshold amplitude for this instability, particularly in magnetic insulators due to their low damping. This allows for efficient excitation of finite-wavevector magnons and the study of nonlinear magnon interactions over a wide power range. However, little is known about how this instability evolves in time and the role of the excitation power. Previous experiments have observed no associated power-dependence [31], or have instead focused on the influence of dipole radiation [32] or of group velocity and proximity to the excitation antenna [33]. The reverse process of splitting is referred to as confluence, which also requires further investigation [33]. Its relationship with splitting is an unresolved question, as is the relationship between three-magnon scattering processes and the magnons' phases.

---

* hamil483@umn.edu

To this end, we employ time-resolved homodyning spectroscopy to examine this instability with phase-sensitivity over five orders of magnitude in microwave excitation power. We observe a regime hosting power-dependent transient oscillations of the FMR amplitude, that at high powers the instability induces $180°$ phase shifts of FMR, and that these phase shifts correspond to reversals between three-magnon splitting and confluence. Furthermore, turning off the microwave excitation stimulates such reversals, generating prolonged and coherent oscillations of the FMR amplitude. Our model is in strong agreement with these observations, and explains the origin of the oscillatory regime as well as the oscillations after turn-off. The oscillatory regime persists up to the highest powers employed, being remarkably robust against the higher-order interactions that arise.

The FMR mode b_0 with a frequency f_0 is subject to the first-order Suhl instability when magnon modes $b_{\pm\mathbf{k}_i}$ at $f_0/2$ are available. This occurs at low FMR frequencies for in-plane magnetized films, due to a minimum in the magnon dispersion [34, 35]; an increase in wavenumber suppresses the dynamic demagnetization field. With these modes available, b_0 becomes unstable above a threshold amplitude and undergoes three-magnon splitting to $b_{\pm\mathbf{k}_i}$. In the reverse process, confluence, two magnons $b_{\pm\mathbf{k}_i}$ combine into a magnon b_0 [Fig. 1(a)].

We investigated this instability in the time domain through homodyning spectroscopy [Fig. 1(b)]. The microwave excitation at the desired FMR frequency f_0 is converted to the desired applied microwave power P_a and to $8\,\mu$s pulses using an attenuator and switch. These pulses enter a wide microstrip waveguide, generating a spatially uniform microwave magnetic field of amplitude h_a throughout the sample: a $3\,\mu$m-thick film of Yttrium Iron Garnet (YIG). We resonantly excite the sample's FMR mode by matching its FMR frequency with f_0, via tuning the static magnetic field H to H_0. We primarily investigated the transient behavior at $f_0 = 1.5$ GHz, with a corresponding resonant field of $H_0 = 135.1$ Oe. The sample is inductively coupled to the microstrip, such that its FMR response b_0 induces a corresponding voltage in the microstrip [36]. We obtain the envelope of the microstrip's output voltage by mixing it with a phase- and frequency-matched reference. By subtracting the output voltage's envelope at resonance from that at zero field, we isolate the envelope of the voltage induced by FMR. When nonlinearity-induced phase shifts are absent, this envelope directly corresponds to the FMR amplitude $c_0(t)$ with the susceptibility $\chi''(t) = c_0(t)/h_a \propto c_0(t)/\sqrt{P_a}$. For additional experimental details, see Sec. 1 of the supplementary

3

material (SM) [37] and Ref. [38] therein.

To verify our experiment, we compare the measured steady-state susceptibility χ''_∞ with Suhl's theory [30] around the instability's threshold power P_S [see Fig. 1(c)]. For $P_a < P_S$, c_0 is in the linear regime, such that its steady-state value is proportional to h_a. For $P_a = P_S$, this value corresponds to c_S, the threshold amplitude for the (nonlinear) instability regime. The steady-state value of c_0 saturates at c_S in the nonlinear regime, as three-magnon splitting occurs for $c_0 > c_S$. As such, as P_a is increased, χ''_∞ decreases as $\chi''_\infty \propto 1/\sqrt{P_a}$. We compare this with the experimental results by normalizing χ''_∞ to its value in the linear regime χ''_L. The experimentally obtained saturation from both steady-state (using lock-in techniques) and time-resolved measurements is in reasonable agreement with the theoretical prediction.

In our time-resolved measurements [Fig. 1(d)], we find both the linear and nonlinear regimes as well as their expected transient behavior: in the linear regime (purple curve) c_0 rises monotonically to its steady-state value, while in the nonlinear regime (blue curve) it becomes unstable and then relaxes to c_S via three-magnon splitting. However, we observe
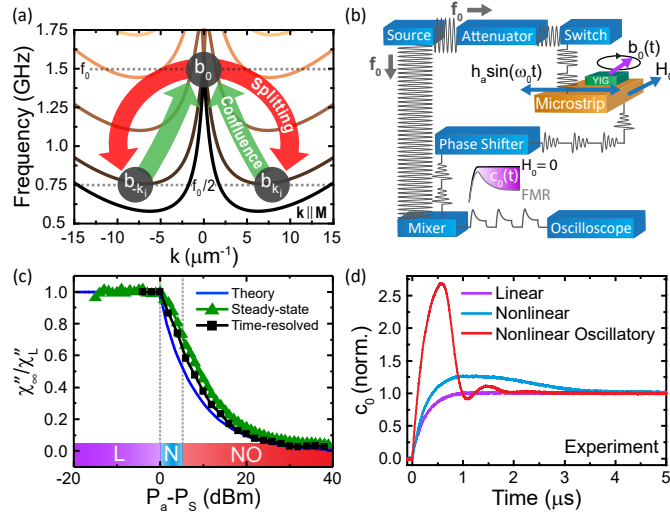

FIG. 1. (a) The magnon dispersion of $3\,\mu$m YIG films magnetized in-plane, in $15°$ increments of the angle between the wavevector $\mathbf{k}$ and the static magnetization $\mathbf{M}$. (b) Schematic diagram of the experiment. (c) $\chi''_\infty(P_a)/\chi''_L$ predicted from Suhl's theory (blue) and that measured through lock-in techniques (green) and time-resolved measurements (black). The color-coded regions correspond to the Linear (L), Nonlinear (N), and Nonlinear Oscillatory (NO) regimes. (d) Overview of the transient behavior of the FMR magnon population c_0 in each regime, normalized to the values of c_0 at steady state.

an additional regime with a threshold power $P_{osc} > P_S$, in which c_0 oscillates at a power-dependent frequency as it relaxes to c_S (red curve).

To understand this regime, we have developed a model for three-magnon scattering of FMR in thin films, for the case of resonant excitation by a perpendicular microwave field (see Sec. 2 of SM [37] for details). We derive the associated equation of motion for the circularly-polarized magnetization m^+ via the Landau-Lifshitz equation. We then perform a plane-wave expansion of m^+ [30] to obtain the equations of motion of the circularly-precessing magnon modes. Afterwards, we employ a classical Bogoliubov transformation [39] to obtain the equations of motion of the eigenmodes, the elliptically-precessing magnon modes $b(\mathbf{k})$. We only retain terms up to second-order in the magnon modes, to account for three-magnon scattering while neglecting higher-order interactions. We account for linear damping of $b(\mathbf{k})$ through the relaxation rate $\eta(\mathbf{k}) = \omega(\mathbf{k})\epsilon(\mathbf{k})\alpha$ [40]; $\omega(\mathbf{k})$ is the mode's angular frequency, $\epsilon(\mathbf{k}) = \frac{1}{\gamma}\left(\partial\omega/\partial H\right)|_{\mathbf{k},H_0}$ is the ellipticity factor, γ is the gyromagnetic ratio, and α is the measured Gilbert damping constant. We only consider the resulting equations of motion of the FMR mode b_0 and the N_k magnon modes $b_{\mathbf{k}_i}$ of frequency $f_0/2$ in the magnon dispersion. Each of these half-frequency modes' equation of motion is distinguished by $\zeta_{\mathbf{k}_i}$, their coupling strength with b_0, and their relaxation rate $\eta_{\mathbf{k}_i}$. However, these distinguishing parameters have weak variation among the $f_0/2$ modes. Hence, we set $\zeta_{\mathbf{k}_i}$ and $\eta_{\mathbf{k}_i}$ to their average value over all $f_0/2$ modes, $\bar{\zeta}, \bar{\eta}_k$. This causes the equations of motion for each of the half-frequency modes to be identical, reducing the N_k half-frequency modes to a single effective mode b_k. Note that we also equate $b_k(t)$ and $b_{-k}(t)$, as the splitting and confluence processes affect each mode equally. This reduces our model to the two equations of motion

$$\dot{b}_0 = (i\omega_0 - \eta_0)b_0 - N_k\bar{\zeta}b_k^2 + \nu h_a e^{i(\omega_0 t - \pi/2)}, \tag{1}$$

$$\dot{b}_k = (i\omega_k - \bar{\eta}_k)b_k + \bar{\zeta}b_k^* b_0. \tag{2}$$

ν is the coupling of b_0 to the microwave field. The magnon mode's response b_i ($i = 0, k$) encodes both its amplitude $|b_i|$ and its phase, such that $b_i(t) = |b_i(t)|e^{i(\omega_i t + \theta_i + \phi_i(t))}$. $\theta_{0,k} = -\pi/2, -\pi/4$ are the modes' phase offsets for the cases of linearity and weak nonlinearity, as found from numerically solving Eqs. (1),(2). $\phi_i(t)$, discussed later, will correspond to phase shifts induced by strong nonlinearity. We define $c_i(t)$ as the mode's amplitude for $\phi_{0,k} = 0$, such that $b_i(t) = c_i(t)e^{i(\omega_i t + \theta_i)}$. Inserting this relation into Eqs. (1),(2) yields the equations
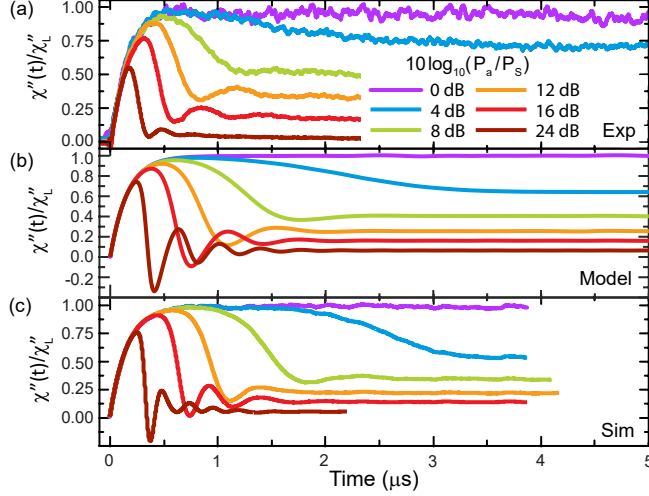
FIG. 2. Comparison of the FMR amplitude's transient behavior from (a) the experiment, (b) the numerical solutions to Eqs. (3),(4), and (c) the micromagnetic simulations. The FMR amplitude c_0 is normalized to $\chi''(t)/\chi''_L$ to enable direct comparison between each approach.

of motion for the magnon mode amplitudes:

$$\dot{c}_0 = -\eta_0 c_0 - N_k \bar{\zeta} c_k^2 + \nu h_a, \tag{3}$$

$$\dot{c}_k = -\bar{\eta}_k c_k + \bar{\zeta} c_k c_0. \tag{4}$$

This definition of c_0, as in the experiment, corresponds to the envelope of b_0 obtained by mixing it with a frequency-matched reference signal $e^{-i(\omega_0 t + \theta_0)}$. As such, the experiment can be directly compared with the numerical solutions of Eq. (3). For numerically solving our equations of motion, we set the value of h_a such that h_a/h_S matches the experiment and simulations; h_S is the observed threshold value of h_a for the instability. η_i is calculated as described previously. All other parameters are set to the values calculated from our model. See Sec. 2 of SM [37] for their derivations. The initial values are the thermal amplitudes corresponding to the Bose-Einstein distribution (see Sec. 3 of SM [37]). For details on the simulations and numerical solutions, see Sec. 4 of SM [37] and Refs. [41–45] therein.

Figure 2 compares the time-evolution of c_0 from the experiment, the numerical solutions of Eqs. (3),(4), and the micromagnetic simulations. We normalize to $\chi''(t)/\chi''_L$ for direct comparison between each approach. Each curve color corresponds to the same relative power P_a/P_S. The purple and blue curves correspond to the linear and nonlinear regimes, while the green curves correspond to the entrance into the nonlinear oscillatory regime. As P_a is increased, the oscillation frequency f_{osc} monotonically increases while the timescale of

the initial transient peak monotonically decreases. Strong qualitative agreement is observed between each approach, which is also the case at 2.5 GHz (see Sec. 5 of SM [37]). The oscillations weaken as one goes from the model to simulation to experiment, presumably due to increasing magnon dephasing. In addition to simulations allowing for other magnon interactions, they include thermal fluctuations which can lead to dephasing. In the experiment, additional dephasing may arise from sample and magnetic field inhomogeneity.

To analyze the oscillatory regime, we linearize Eqs. (3),(4) by Taylor expanding $\dot{c}_0, \dot{c}_k$ about the nonlinear regime's fixed point, which corresponds to steady state; this allows us to treat the second-order terms as negligible. We then impose a time-dependence of the form $c_0, c_k \propto e^{\lambda t}$, and solve for λ. The transition to the oscillatory regime corresponds to the nonlinear regime's fixed point changing from a stable node to a stable spiral, such that λ becomes complex. This transition can be thought of as the point where the splitting rate becomes large enough to produce negative feedback by suppressing c_0 to below c_S, where splitting is suppressed. This generates exchanges in dominance between the splitting and the microwave excitation terms in Eq. (3), hence the oscillations. This analysis (see Sec. 6 of SM [37]) yields predicted values for the oscillation frequency f_{osc} and the threshold value of h_a for the oscillatory regime, h_{osc}:

$$f_{osc} = \eta_0 \sqrt{\frac{\bar{\zeta}\nu}{8\pi^2}(h_a - h_{osc})}, \tag{5}$$

$$h_{osc} = h_S(1 + \frac{\eta_0}{8\bar{\eta}_k}). \tag{6}$$

We compare the predicted scaling from Eq. (5) with our results by extracting, via a Fourier transform, the oscillations' frequency spectra from each approach [Figs. 3(a,b)]. We define f_{osc} at each power as the characteristic peak in the oscillations' frequency spectra and h_{osc} as the value of h_a just below where low-frequency structure is observed in the spectra. For more details, see Sec. 7 of SM [37]. The linearized model's predicted scaling $f_{osc} \propto \tilde{h}^{0.5}$, where $\tilde{h} = (h_a - h_{osc})/h_{osc}$, is compared to the scaling obtained from each approach [Fig. 3(c)]. We normalize $h_a - h_{osc}$ by h_{osc} to directly compare each approach. The model's results are from the numerical solutions of Eqs. (3), (4). The filled symbols are those included in the scaling fit (dashed lines) such that quantitative agreement with Eq. (5) is observed. The range of agreement for each approach is several orders of magnitude in P_a. This is also the case for $f_0 = 2.5$ GHz (see Sec. 5 of SM [37]). The oscillation frequencies in the experiment and simulations show good agreement, but they are larger than those from our

model. This is likely due to an incomplete treatment of damping and/or an underestimation of $\bar{\zeta}$, as we neglect the full Gilbert damping term and spatial variation of the longitudinal magnetization component.

As the relative power $10\log_{10}(\mathrm{P_a/P_{osc}})$ increases to 14 dB, the oscillations' frequency spectra broaden in the experiment and simulations [Figs. 3(a,b)]. To investigate this, we compare the simulations' magnon mode amplitudes $c(\mathbf{k})$ [46] at the relative powers of 2 dB (no broadening) and 25 dB (pronounced broadening) [Fig. 3(d)]. At 2 dB, only the $f_0/2$ modes with the largest coupling strengths $\zeta_{\mathbf{k}_i}$ are excited. Note that the coupling is strongest for the modes with wavevectors most misaligned with the static magnetization $\mathbf{M}$. At 25 dB, the weaker-coupled $f_0/2$ modes are also excited, with some even exceeding the amplitude of the strongest-coupled modes. The excited modes also exhibit a wider frequency distribution about $f_0/2$, which may generate the observed broadening. The most straightforward explanation for this transition is the onset of four-magnon scattering of $f_0/2$, opposite-wavevector pairs of magnons at the strongest-coupled modes to such pairs at
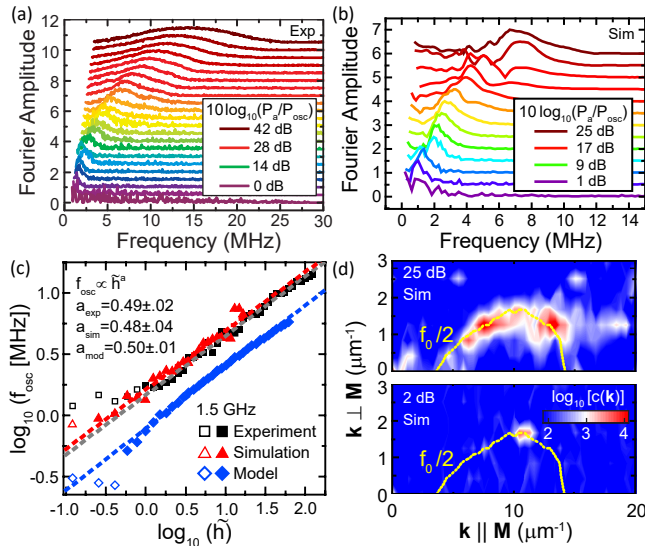

FIG. 3. Oscillation analysis at $f_0 = 1.5$ GHz. (a,b) Normalized and offset frequency spectra of the oscillations in (a) the experiment, and (b) the simulations, with a 2 dB increment between curves. (c) The scaling of the oscillation frequency f_{osc} for each approach. The filled symbols indicate the fitted region and have a spacing of 1 dB in power. (d) The simulations' magnon mode amplitudes $c(\mathbf{k})$ for powers 2 dB (bottom, no broadening) and 25 dB (top, with broadening) greater than P_{osc}.

weaker-coupled modes, which conserves energy and momentum.

At the highest powers, the splitting becomes pronounced enough to introduce negative values of c_0 [Figs. 4(a,b)]. As c_0 is phase-sensitive, being obtained by mixing b_0 with a reference signal, this corresponds to b_0 undergoing a phase shift $\phi_0 \sim 180°$. Phase shifts for the mode b_i arise when its response is dominated by its scattering term [see Eqs. (1),(2)], such that it is strongly nonlinear. At these powers, we also observe pronounced oscillations of c_0 after turning off the microwave excitation. Notably, these oscillations' amplitudes greatly exceed the steady-state value of c_0 during excitation and they persist for roughly 600 ns. Each curve in Figs. 4(a,b) is normalized to the turn-on peak at the highest power, showing the oscillations at excitation turn-on and turn-off to be comparable in size. To understand these observations, we examine the case of strong nonlinearity in our model by numerically solving Eqs. (1),(2), which provides the evolution of the modes' amplitudes as well as their phases. We calculate the modes' phase shifts $\phi_i(t)$ by using our general definition $b_i(t) = |b_i(t)|e^{i(\omega_i t + \theta_i + \phi_i(t))}$:

$$\phi_i(t) = \frac{1}{i}\ln\left(\frac{b_i(t)}{|b_i(t)|}e^{-i(\omega_i t + \theta_i)}\right). \tag{7}$$

The evolution of the amplitudes and phase shifts is shown in Figs. 4(c,d) and Figs. 4(e,f); we utilize $|\phi_i(t)|$ for simplicity. For consistency with the experiment, we plot c_0 instead of $|b_0|$, taking $c_0(t) = \text{Re}(b_0(t)e^{-i(\omega_0 t + \theta_0)})$.

After turning on the excitation [Figs. 4(c,e)], we find π phase shifts of ϕ_0 at $c_0 = 0$, with these phase shifts triggering variation in ϕ_k. We first examine the influence of the π phase shift on the amplitudes' equations of motion. Whereas $c_i(t)$ is the mode's amplitude for $\phi_{0,k} = 0,0$, we define $c_i'(t)$ as the mode's amplitude for $\phi_{0,k}' = \pi, 0$. Substituting $b_i(t) = c_i'(t)e^{i(\omega_i t + \theta_i + \phi_i')}$ into Eqs. (1),(2) yields the amplitudes' new equations of motion given the π phase shift:

$$\dot{c}_0' = -\eta_0 c_0' + N_k \bar{\zeta} c_k'^2 - \nu h_a, \tag{8}$$

$$\dot{c}_k' = -\bar{\eta}_k c_k' - \bar{\zeta} c_k' c_0'. \tag{9}$$

Comparison with Eqs. (3),(4) shows that the π phase shift switches the sign of both the microwave field term νh_a and the three-magnon scattering terms $\sim \bar{\zeta}$. From the latter, it is evident that these phase shifts correspond to reversals in the three-magnon scattering direction between splitting and confluence. These reversals explain why the phase shifts
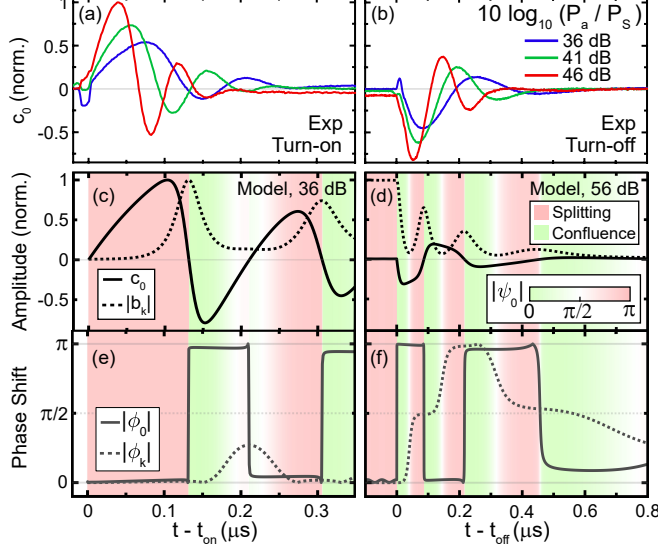
FIG. 4. (a,b) The experimental results for $c_0(t)$ at high powers when turning on and off the microwave excitation. Each curve is normalized to the peak amplitude at turn-on for the relative power of 46 dB. (c,d) The magnon amplitudes c_0, $|b_k|$, with each time color-coded for the corresponding value of $|\psi_0|$. Note that c_0 at turn-off is instead normalized to the peak amplitude at turn-on for the relative power of 56 dB. (e,f) The corresponding phase shifts $|\phi_{0,k}|$.

cause $|b_k(t)|$ to switch between growing and decaying with time, and why $|c_0(t)|$ increases with time for $c_0 < 0$ despite being out-of-phase with (and hence, damped by) the microwave field [Figs. 4(a,c)]. Furthermore, the reversals explain the variation of ϕ_k: with $|b_k(t)|$ being suppressed by confluence, its three-magnon scattering term dominates over its linear terms such that b_k enters the strong nonlinearity regime.

These reversals are more directly evident after turning off the microwave excitation, where $|c_0(t)|$ undergoes a pronounced increase in time despite the absence of the excitation field. Furthermore, without the microwave field to drive ϕ_0 back to $0°$, the variations of ϕ_k evolve into $90°$ phase shifts of b_k, generating additional reversals [Figs. 4(d,f)]. The $180°, 90°$ phase shifts of b_0, b_k are those required to reverse the scattering direction, with the factor-of-two difference being due to the same factor difference in their frequencies. These reversals explain both the pronounced oscillations of c_0 at turn-off and the oscillations' enhancement with microwave power: the scattering at turn-off, and hence the reversals, are driven by the steady-state values of c_0, c_k during turn-on, where $c_k \propto \sqrt{h_a - h_S}$ at steady state [see Eq. 51 in SM [37]]. The model's turn-off oscillations of c_0 are much weaker than those in the

10

experiment, hence the use of the higher relative power of 56 dB. This may be because of our use of a linear damping term $-\eta_i b_i$, which is insensitive to phase shifts, instead of the full Gilbert damping term.

To determine how the scattering direction evolves in time, we consider the relative phase $|\psi_i(t)|$ between b_i and the three-magnon scattering term in its equation of motion. As with the linear damping term $-\eta_i b_i$, the damping of b_i by scattering corresponds to the scattering term being π out-of-phase with b_i. Conversely, the scattering term drives b_i when it is in-phase with b_i. As such, $|\psi_0| = 0, \pi$ corresponds to confluence and splitting, respectively, and we can calculate $|\psi_0(t)|$ to determine the evolution of the scattering direction. Note that $|\psi_0(t)|$ and $|\psi_k(t)|$ are found to mirror each other about $\pi/2$ as expected, such that one mode is being driven by scattering while the other mode is being damped. From Eq. (1), $\psi_0(t)$ takes the form

$$\psi_0(t) = \frac{1}{i}\ln\left(\frac{b_0(t)/|b_0(t)|}{b_k^2(t)/|b_k^2(t)|}\right).\tag{10}$$

$|\psi_0(t)|$ corresponds to the color-coding in Figs. 4(c-f). The switching of $|\psi_0(t)|$ between $0, \pi$ aligns with the phase shifts and the transitions between growth and decay of $|b_k(t)|$ as expected, verifying that the relative phase $|\psi_i(t)|$ indicates the three-magnon scattering direction.

In summary, for three-magnon scattering of ferromagnetic resonance, we observe a regime that hosts transient oscillations of the magnon populations, with the transient behavior being highly dependent on the excitation power. At high excitation powers, we find that the scattering generates significant phase shifts of the magnons and that these phase shifts correspond to reversals between three-magnon splitting and confluence. Such reversals also occur upon turning off the excitation, generating prolonged and coherent oscillations. Our model captures these behaviors. These findings shed light on the transient behavior of this instability, and reveal the nontrivial interplay between three-magnon scattering and the magnons' phases.

—————————————————————

[1] S.M. Rezende and F.M. de Aguiar, Spin-wave instabilities, auto-oscillations, and chaos in yttrium-iron-garnet, Proc. IEEE **78**, 893 (1990).

[2] P. Wigen, R. McMichael, and C. Jayaprakash, Route to chaos in the magnetic garnets, J. Magn. Magn. **84**, 237 (1990).

[3] I. Laulicht and P. Wigen, On the transient and stationary parametric excitation of spin waves, J. Magn. Magn. **207**, 103 (1999).

[4] C. Mathieu, V.T. Synogatch, and C.E. Patton, Brillouin light scattering analysis of three-magnon splitting processes in yttrium iron garnet films, Phys. Rev. B **67**, 104402 (2003).

[5] S.Y. An, P. Krivosik, M.A. Kraemer, H.M. Olson, A.V. Nazarov, and C.E. Patton, High power ferromagnetic resonance and spin wave instability processes in Permalloy thin films, J. Appl. Phys. **96**, 1572 (2004).

[6] P. Kabos, G. Wiese, and C. Patton, Measurement of spin wave instability magnon distributions for subsidiary absorption in yttrium iron garnet films by Brillouin light scattering, Phys. Rev. Lett. **72**, 2093 (1994).

[7] A. Krawiecki and A. Sukiennicki, On-off intermittency and peculiar properties of attractors in a simple model of chaos in ferromagnetic resonance, Acta Phys. Pol. A **2**, 269 (1995).

[8] T.L Carroll, L.M Pecora, and F.J Rachford, Chaos in magnetostatic modes in an yttrium iron garnet film between 2 and 4 GHz, J. Appl. Phys. **67**, 5630 (1990).

[9] T.L Carroll, L.M Pecora, and F.J Rachford, Chaos and chaotic transients in an yttrium iron garnet sphere, Phys. Rev. A **40**, 377 (1989).

[10] T.L Carroll, L.M Pecora, and F.J Rachford, Chaotic transients and multiple attractors in spin-wave experiments, Phys. Rev. Lett. **59**, 2891 (1987).

[11] W. Araujo, F. de Aguiar, A. Azevedo, and S. Rezende, Dual pumping of magnetostatic and spin-wave modes in yttrium–iron–garnet spheres, J. Appl. Phys. **93**, 8752 (2003).

[12] G. Srinivasan, M. Chen, and C. Patton, Observation of auto-oscillations and chaos in sub-

sidiary absorption in yttrium iron garnet, J. Appl. Phys. **64**, 5480 (1988).

[13] V.E. Zakharov, V. L'vov, and S. Starobinets, Spin-wave turbulence beyond the parametric excitation threshold, Sov. Phys. Uspekhi **17**, 896 (1975).

[14] V.B Cherepanov and A.N Slavin, Collective spin-wave oscillations in finite-size ferromagnetic samples, Phys. Rev. B **47**, 5874 (1993).

[15] S. Rezende, F. de Aguiar, and A. Azevedo, Spin-wave auto-oscillations still in need of a good model, J. Appl. Phys. **67**, 5624 (1990).

[16] A.N Slavin, G. Srinivasan, S. Cordone, and V.B Cherepanov, Instability mechanism of collective spin wave oscillations in finite-size ferrite samples, J. Appl. Phys. **75**, 5610 (1994).

[17] V.T. Synogach, Y.K. Fetisov, C. Mathieu, and C.E. Patton, Ultrashort microwave pulses generated due to three magnon interactions, Phys. Rev. Lett. **85**, 2184 (2000).

[18] Roman V. Verba, Lukas Körber, Katrin Schultheiss, Helmut Schultheiss, Vasil Tiberkevich, and Andrei N. Slavin, Theory of three-magnon interaction in a vortex-state magnetic nanodot, Phys. Rev. B **103**, 014413 (2021).

[19] I. Barsukov, H.K. Lee, A.A. Jara, Y.-J. Chen, A.M. Gonçalves, C. Sha, J.A. Katine, R.E. Arias, B.A. Ivanov, and I.N. Krivorotov, Giant nonlinear damping in nanoscale ferromagnets, Sci. Advc. **5**, eaav6943 (2019).

[20] K. Schultheiss, R. Verba, F. Wehrmann, K. Wagner, L. Körber, T. Hula, T. Hache, A. Kákay, A.A. Awad, V. Tiberkevich, A.N. Slavin, J. Fassbender, and H. Schultheiss, Excitation of whispering gallery magnons in a magnetic vortex, Phys. Rev. Lett. **122**, 097202 (2019).

[21] T.X. Zhou, J.J. Carmiggelt, L.M. Gächter, I. Esterlis, D. Sels, R.J. Stöhr, C. Du, D. Fernandez, J.F. Rodriguez-Nieva, F. Büttner, E. Demler, and A. Yacoby, A magnon scattering platform, Proc. Nat. Acad. Sci. USA **118**, e2019473118 (2021).

[22] A.A. Serga, A.V. Chumak, B. Hillebrands, YIG magnonics, J. Phys. D **43**, 264002 (2010).

[23] J.D. Adam and S.N. Stitzer, Frequency selective limiters for high dynamic range microwave receivers, IEEE Trans. Microw. Theory Tech. **41**, 2227 (1993).

[24] J.D. Adam and F. Winter, Magnetostatic wave frequency selective limiters, IEEE Trans. Magn. **49**, 956 (2013).

[25] P. Pirro, V.I. Vasyuchka, A.A. Serga, and B. Hillebrands, Advances in Coherent Magnonics, Nat. Rev. Mater. **6**, 11141135 (2021).

[26] A. Barman, G. Gubbiotti, S. Ladak, A.O. Adeyeye, M. Krawczyk, J. Gräfe, C. Adelmann,

S. Cotofana, A. Naeemi, V.I. Vasyuchka, *et al.*, The 2021 magnonics roadmap, J. Phys. Condens. Matter (2021).

[27] G. Csaba, Á. Papp, and W. Porod, Perspectives of using spin waves for computing and signal processing, Phys. Lett. A **381**, 1471 (2017).

[28] A.V. Chumak, Magnon spintronics: Fundamentals of magnon-based computing, in *Spintronics Handbook: Spin Transport and Magnetism, Second Edition* (CRC Press, 2019) pp. 247–302.

[29] A. Etesamirad, R. Rodriguez, J. Bocanegra, R. Verba, J. Katine, I. Krivorotov, V. Tyberkevych, B. Ivanov, and I. Barsukov, Controlling Magnon Interaction by a Nanoscale Switch, ACS Appl. Mater. Interfaces **13**, 20288-20295 (2021).

[30] H. Suhl, The theory of ferromagnetic resonance at high signal powers, J. Phys. Chem. Solids **1**, 209 (1957).

[31] R. Cunha, J. Holanda, L. Vilela-Leão, A. Azevedo, R. Rodríguez-Suárez, and S. Rezende, Nonlinear dynamics of three-magnon process driven by ferromagnetic resonance in yttrium iron garnet, Appl. Phys. Lett. **106**, 192403 (2015).

[32] B. Desormiére, E. Milot, and H. Le Gall, Transient processes in spin-wave systems with magnetic dipole radiation-II. Experimental investigations*, J. Phys. Chem. Solids **30**, 1135-1146 (1969).

[33] H.J. Liu, G.A. Riley, C.L. Ordóñez-Romero, B.A. Kalinikos, and K.S. Buchanan, Time-resolved study of nonlinear three-magnon processes in yttrium iron garnet films, Phys. Rev. B **99**, 024429 (2019).

[34] B. Kalinikos and A.N Slavin, Theory of dipole-exchange spin wave spectrum for ferromagnetic films with mixed exchange boundary conditions, J. Phys. C **19**, 7013 (1986).

[35] M. Mansuripur and R. Giles, Demagnetizing field computation for dynamic simulation of the magnetization reversal process, IEEE Trans. Magn. **24**, 2326 (1988).

[36] I.S. Maksymov and M. Kostylev, Broadband stripline ferromagnetic resonance spectroscopy of ferromagnetic films, multilayers and nanostructures, Physica E Low Dimens. Syst. Nanostruct. **69**, 253 (2015).

[37] See Supplemental Material at [URL will be inserted by publisher] for information on the methods and analyses employed, the derivation and linearization of our model, the calculation of the initial magnon amplitudes, and companion data at 2.5 GHz FMR frequency.

[38] Matesy GMBH, https://matesy.de/en/products/materials/yig-films.

[39] A. Y. Dobin and R. H. Victora, Intrinsic nonlinear ferromagnetic relaxation in thin metallic films, Phys. Rev. Lett. **90**, 167203 (2003).

[40] V. Kambersky and C. E. Patton, Spin-wave relaxation and phenomenological damping in ferromagnetic resonance, Phys. Rev. B **11**, 2668 (1975).

[41] Y.-H. Tang, N. Kioussis, A. Kalitsov, W. Butler, and R. Car, Influence of asymmetry on bias behavior of spin torque, Phys. Rev. B **81**, 054437 (2010).

[42] N. A. Natekar, W.-H. Hsu, and R. H. Victora, Calculated dependence of FePt damping on external field magnitude and direction, AIP Adv. **7**, 056004 (2017).

[43] W. F. Brown, Fluctuations of a single-domain particle, Phys. Rev. **130**, 1677 (1963).

[44] Z. Liu, P.-W. Huang, G. Ju, and R. H. Victora, Thermal switching probability distribution of L10 FePt for heat assisted magnetic recording, Appl. Phys. Lett. **110**, 182405 (2017).

[45] A. Venugopal, T. Qu, and R. H. Victora, Non-linear parallel pumped FMR: Three and Four magnon processes, IEEE Trans. Microw. Theory Tech. **68**, 602 (2020).

[46] T. Qu, A. Venugopal, J.M. Etheridge, W.K. Peria, K. Srinivasan, B.J. Stadler, P.A. Crowell, and R.H. Victora, Nonlinear magnon scattering mechanism for microwave pumping in magnetic films, IEEE Access **8**, 216960 (2020).